

Experimental and numerical modelling of picosecond laser ablation of thin aluminium Polyethylene Terephthalate (PET) films

Tong Zhou¹, Zheng Fang¹, Walter Perrie^{1*}, Yang Fei¹, Stuart Edwardson¹ and Geoff Dearden¹

¹ Laser Group, School of Engineering, University of Liverpool, Brownlow Street, Liverpool L69 3GH, UK

Email: wpfemto1@liverpool.ac.uk

Abstract

An experimental and theoretical study on 10 ps single pulse ablation of 10 – 50 nm aluminium films on Polyethylene Terephthalate (PET) substrate has been carried out. Both front and rear side ablation with different film thicknesses were measured experimentally and modelled numerically. It was found that the ablation threshold varied linearly with film thickness between 10 nm to 50 nm and showed a reasonable experimental and theoretical agreement. The rear side ablation threshold is always lower than the front side, with tearing at the edges. The front and rear side ablation thresholds for a 10 nm thick film were measured to be $F_{th}(f) = 0.021 \pm 0.008 \text{ Jcm}^{-2}$ and $F_{th}(r) = 0.016 \pm 0.002 \text{ Jcm}^{-2}$ respectively, with a ratio of $F_{th}(f)/F_{th}(r) \sim 1.3$. This ratio drops to ~ 1.1 with 50 nm films. The maximum electron temperature of the aluminium is also related to the film thickness. The highest electron temperature appears with the thinnest film, optical density = 0.5, $t \sim 10 \text{ nm}$, reaching $T_e \sim 7,600\text{K}$ under fluence $F = 0.20 \text{ Jcm}^{-2}$ at a delay time $t = 13 \text{ ps}$ while the thermal equilibrium is established at $\sim 30 \text{ ps}$. There is also a temperature gradient at the Al/PET interface due to the electron insulation and the sharp transition of the Al and PET thermal diffusivity. With a PET damage threshold, $F_{th, PET} = 3.46 \text{ Jcm}^{-2}$, a clear processing window avoiding PET substrate damage was observed in single pulse exposure, and multi-beam parallel processing with the aid of a spatial light modulator was demonstrated, accelerating film patterning significantly.

Keywords: Ultrafast laser, thin-film ablation, two-temperature model, metal-nonmetal interface, PET substrate

1. Introduction

Ultrashort laser ablation has demonstrated the capability to obtain high-speed, high quality and precise micromachining on various materials, including thin metal films [1-4]. For example, laser patterned thin metal film of Ni/Cr, Mo, Ag, Al and Pt on glass, polyethylene terephthalate (PET), polyimide (PI), or poly-methyl methacrylate (PMMA) has been employed on sensors, solar cells and displays [4-8]. Unlike bulk materials, the film thickness is a critical parameter during the ablation as the effective penetration depth, which depends on the material optical and thermal properties at a given laser wavelength, is no longer small compared with materials thickness [9]. Also, the substrate can increase the ablation efficiency of the thin film [9-11]. In this case, a clear understanding of the ultrafast laser removal of the metal thin film mechanism is necessary.

For ultra-short pulse laser ($< 10 \text{ ps}$) ablation, the energy is first absorbed by conduction electrons then transported to the lattice via electron-phonon interactions, leading to a nonequilibrium temperature stage [12]. This nonequilibrium makes the conventional heat conduction equation (Fourier law) no longer valid. Thus, the model involving the nonequilibrium heat transfer between electrons and lattice, called the two-temperature model (TTM), is well accepted in ultrafast laser ablation [13].

There is a wide range of research on bulk or single-layer material ablation modelling based on TTM. Kumar et al. [14] simulated a single-shot laser ablation on Ti6Al4V alloy, predicting the ablation threshold and depth with 100 fs temporal pulse length and 1064 nm wavelength. Similarly, single and multiple pulse ablation on bulk stainless steel and aluminium film was investigated by Wang et al.[15] and Li et al. [16], respectively. They both predicted the ablated depth and crater radii under the single /multi pulse ablation, and there is a nearly linear relationship between the ablated depth and pulse number for multi-pulse ablation. Olbrich et al. [17] has also carried out similar work of different

thickness aluminium films on a glass substrate, and a ‘gentle’ and ‘strong’ ablation effect was found when the film thickness was greater than 100 nm.

However, the ablation of multilayered materials is more complex as different boundary conditions need to be considered. The differing material properties lead to an abrupt change of physical parameters at the interface of the layers [10, 18-20]. Metal to metal films allows continuous heat conduction across the interface, while a more complicated case should be included in metal-nonmetal films [21]. Zhou et al. [10] set insulation of electrons and thermal contact of the lattice as boundary conditions at the gold/glass interface since there are few free electrons in dielectric materials. Majumdar et al. [20] illustrated the nonequilibrium heat transfer between the electron and phonon at the metal-nonmetal interface. Therefore, due to the challenge of modelling thin film systems along with current technical requirements, the study on the ultrafast laser interactions on multilayered materials, especially for metal-nonmetal interfaces, needs to be explored.

The experimental and numerical study on single-pulse ultrafast laser ablation on Al coated PET is presented here. The influence of the film thickness and the PET substrate on the ablation threshold is discussed, based on TTM model.

2. Experimental setup

A schematic of the experimental system is shown in Figure 1. A halfwave plate and Glan laser polariser attenuated the linear polarised output beam from a Nd:VAN seeded regenerative amplifier (High-Q IC-355-800 ps, 10 ps/1064nm). Then the beam was expanded through a diffraction-limited telescope ($M \sim \times 3$), and two plane mirrors were used to maintain a low angle of incidence (AOI) on a reflective phase-only spatial light modulator (SLM) (Hamamatsu-10468-03). A correction field computer generated hologram (CGH to compensate SLM flatness) was applied to the SLM. Then the laser passed through a 4f optical system ($f_1 = f_2 = 400$ mm) to the input aperture of a galvo system (Nutfield XLR8-10) via a periscope and was focussed by a flat-field f-theta lens ($f = 100$ mm). A fast mechanical shutter (Thorlabs SH05) allowed the pulse number on target to be varied, which is synchronised to the scanning software. Al/PET samples were taped on a kinematic mirror mount with vertical drive (Thorlabs, VM1/M), in which case the film could be stretched flat and allow any transmitted laser light to diverge below the surface. The mount was placed on a 3-axis (x, y, z) Aerotech micro-positioning system to precisely control the sample’s focal position. The pulse energy was calibrated under the galvo using a power meter (Coherent, LM-3). Five times measurements were carried out for each experiment. A Nikon DS-U2 which is the camera control unit, coupled with the microscope and NIS-Element D software, was used to measure the ablated crater radius. Multi-spot parallel processing was also demonstrated with appropriate CGH applied to the SLM.

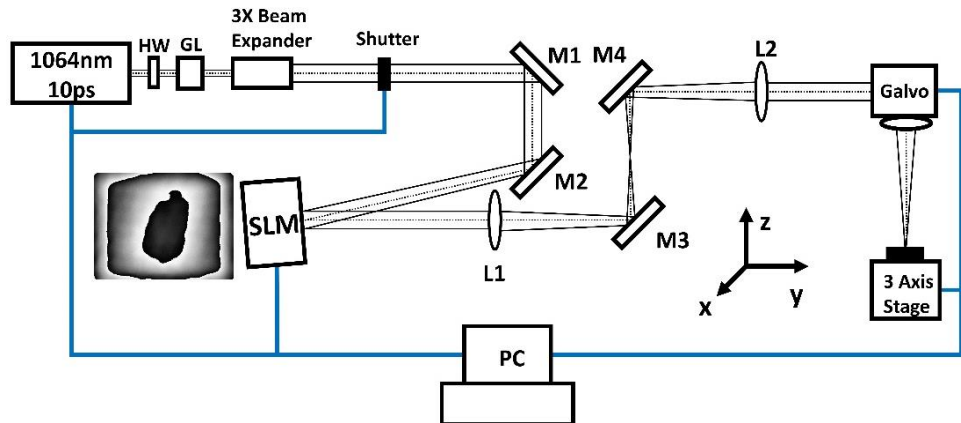


Figure 1. Schematic of the experimental setup. The expanded beam is directed at low AOI to the SLM, then reimaged to the input aperture of scanning galvo with a 4f system. A flatness correction CGH is applied to SLM

3. Numerical Modelling

3.1 Two temperature model

The well-known two-temperature model (TTM) [13] is set for solving the electron and lattice temperature in spatial and time distributions. For the axisymmetric 2-D case, the model is presented below:

$$C_e \frac{\partial T_e}{\partial t} = \nabla \cdot (k_e \nabla T_e) - G(T_e - T_l) + S(r, z, t) \quad (1)$$

$$C_l \frac{\partial T_l}{\partial t} = \nabla \cdot (k_l \nabla T_l) + G(T_e - T_l) \quad (2)$$

$$\nabla = \left[\frac{\partial}{\partial r}, \frac{\partial}{\partial z} \right] \quad (3)$$

where C_e/C_l and k_e/k_l represent the heat capacity and thermal conductivity of electron and lattice, respectively. T_e and T_l are the temperatures of electron and lattice, G is the electron-lattice coupling coefficient, and $S(r, z, t)$ represents the absorbed laser heating source which can be described as [22]:

$$S(r, z, t) = (1 - R) \frac{F}{t_p} \exp\left(-2 \frac{r^2}{r_0^2}\right) \cdot \exp\left(2.77 \frac{(t-t_p)^2}{(t_p)^2}\right) \exp(-\alpha z) \quad (4)$$

in which F is laser fluence, R is material reflectivity, t_p is pulse length FWHM, r_0 is the $1/e^2$ radius of the laser beam, α is the absorption coefficient of aluminium, while r, z, t represents the radius, depth and time variation of Gaussian laser intensity distribution.

In this model, the electron heat capacity C_e is linearly proportional to the electron temperature, and electron thermal conductivity is obtained below [23] :

$$C_e = kT_e \quad (5)$$

$$k_e = k_0 \frac{\left(u_e^2 + 0.16\right)^{\frac{5}{4}} \cdot (u_e^2 + 0.44) \cdot u_e}{\left(u_e^2 + 0.092\right)^{\frac{1}{2}} \cdot (u_e^2 + b \cdot u_l)} \quad (6)$$

k is electron heat capacity at room temperature, k_0 is the constant of electron thermal conductivity, $u_e = T_e/T_f$ and $u_l = T_l/T_f$, b is electron thermal conductivity material constant, and T_f is Fermi temperature of aluminium ($T_{f,Al} = 1.349e5$ K). Also, electron-lattice coupling factor G is given as [10]:

$$G = g_0 \left[\left(\frac{A}{B} \right) (T_e + T_l) + 1 \right] \quad (7)$$

where A and B are material constants, g_0 is the electron-phonon coupling factor at room temperature.

The numerical change of the phase state is considered by combining the latent heat of fusion H_M and vaporisation H_V in the volumetric heat capacity of the lattice [17],

$$C_l = \rho \cdot \left[c_{l0} + \frac{H_M}{\Delta T \cdot \sqrt{2\pi}} \cdot e^{-\frac{1}{2} \left(\frac{T_l - T_M}{\Delta T} \right)^2} + \frac{H_V}{\Delta T \cdot \sqrt{2\pi}} \cdot e^{-\frac{1}{2} \left(\frac{T_l - T_V}{\Delta T} \right)^2} \right] \quad (8)$$

C_{l0} represents the heat capacity constant of the material, and $\Delta T = 50$ K is used, which determines the width of the zone of phase change. T_M and T_V are the melting and vaporisation temperature, respectively.

The reflectivity of the material depends on irradiation laser wavelength, temperature and film thickness, and it can be expressed as a function of refractive index n and extinction coefficient κ at a certain wavelength [24]:

$$R = \frac{(n - 1)^2 + \kappa^2}{(n + 1)^2 + \kappa^2} \quad (9)$$

where, at 1064 nm, $n = 1.3763$ and $\kappa = 10.245$, gives reflectivity as $R = 0.94$ (solid) [24], and drops to 0.88 when aluminium becomes liquid after approximately 2 ps [25]. Hass et al. [26] pointed out that the total absorption of a thin aluminium film almost remained unchanged down to 10 nm thickness for extremely fast evaporation. Also, a study on 40 fs pulse laser ablation of 1 μm thickness aluminium film shows the solid-to-liquid transition took place only in 1.5-2 ps [27]. In this case, the front side absorption of all Al/PET films was considered to be a constant $A_f = (1-R) = 1 - 0.88 = 0.12$. On the other hand, rear side exposure of the air/PET and PET/Al interfaces infers a different effective reflectivity as follows. The PET surface reflectivity ($n = 1.5481$ at 1064 nm [28]) $R_1 = 0.046$ at the Air/PET interface. As the Al melts rapidly on exposure at the PET/Al interface and using complex reflective index (RI) of liquid Al, $\varepsilon_{1.1\mu\text{m}} = 3.35 + 9.37i$ [25], the effective reflectivity at Al/PET interface is $R_2 = [(3.35 - 1.548)^2 + 9.37^2] / [(3.35 + 1.548)^2 + 9.37^2] = 0.815$. Combining these reflectivities, transmission of laser light to the aluminium surface yields an absorption factor in the rear side ablation $A_r = (1 - R_1)(1 - R_2) = 0.177 > 0.12$ of the front side ablation.

3.2 Axisymmetric model building

A 2D axisymmetric finite element model with a mesh size of 100 nm * 1 nm (r and z-direction respectively) of various thicknesses of the aluminium layer and 100 nm * 10 nm mesh size of a 25 μm * 1 μm PET layer is built to simulate single-pulse laser ablation of Al/PET film system. This two-layer system is symmetric to the laser beam axis, simplifying the computations used in COMSOL Multiphysics 5.2. The thickness of aluminium film is set according to the experimental measurement, and a 1 μm PET layer is computed in this model due to the low thermal diffusivity $D_{\text{PET}} = 0.001 \text{ cm}^2\text{s}^{-1}$ [29] and heat diffusion depth $\sqrt{2D_{\text{PET}}t_p} \sim 1.4 \text{ nm}$ of PET. Moreover, PET is nearly transparent in the visible and NIR wavelength with an absorption coefficient $\alpha_{\text{PET}} = 0.133 \text{ cm}^{-1}$ [28] at 1064 nm. In this case, only thermal conduction is considered in the PET layer.

The Al/PET interface is set as an electron insulator as there are a few free electrons in polymer materials (PET). Therefore, Al/PET interface is set as an insulated boundary of electrons and thermal contact boundary of the lattice. Heat flow at Al/PET interface is continuous when thermal resistance is considered for the PET lattice. Therefore, the boundary condition at Al/PET interface is described below [10]:

$$\nabla \cdot (k_e \nabla T_e) = 0 \quad (10)$$

$$-\nabla \cdot (k_{l, \text{Al}} \nabla T_{l, \text{Al}})|_{\text{interface}} = -\nabla \cdot (k_{l, \text{PET}} \nabla T_{l, \text{PET}})|_{\text{interface}} \quad (11)$$

The PET lattice temperature can be described by,

$$C_{l, \text{PET}} \frac{\partial T_{l, \text{PET}}}{\partial t} = \nabla \cdot (k_{l, \text{PET}} \nabla T_{l, \text{PET}}) \quad (12)$$

This computation was performed over a hundred picosecond time interval. In this case, the lattice thermal conduction and traditional boundary heat loss can be ignored while zero flux boundary condition was applied on the right-hand side (well beyond the laser beam radius) and bottom sides. Initial values of temperature and ambient pressure were set as $T_0 = 293 \text{ K}$ and 1 bar. The front side and rear side ablation cases are investigated, in which electron insulation was set on Al/PET interface as shown in Figure 2 (a) and (b). Laser and material parameters are listed in Table 1.

Table 1. Laser parameters and thermos-physical properties of aluminium [11, 17, 30, 31]

Parameter	Value	
Laser parameters	Laser fluence F [J/cm ²] Wavelength λ [nm] Radius w_0 [μm] Pulse duration t_p [ps]	0.2, 0.6 1064 14.8 10
Thermo-physical parameters of aluminium	Coefficient of electron heat capacity k [J m ⁻³ K ⁻¹] Front side absorption A_f Rear side absorption A_r Absorption coefficient α [m ⁻¹] Specific heat capacity C_{10} [J kg ⁻¹ K ⁻¹] Thermal conductivity k_0 [W m ⁻¹ K ⁻¹] Material constant for electron relaxation time A [s ⁻¹ K ⁻²] Material constant for electron relaxation time B [s ⁻¹ K ⁻¹] Electron thermal conductivity material constant b Fermi Temperature T_f [K] Electron-lattice coupling at room temperature g_0 [W m ⁻³ K ⁻¹] Melting temperature T_m Al [K] Evaporation temperature, T_v Al [K] Latent heat of fusion, H_M [kJ/kg] Evaporation enthalpy, H_v [kJ/kg] Density, ρ_{Al} [kg m ⁻³]	134.5 0.12 0.177 1.2e8 903 235 0.376e7 3.9e11 0.48 1.349e5 2.45e17 933.5 2743 399 10530 2702
Thermo-physical parameters of PET	Thermal conductivity, k_{PET} [W m ⁻¹ K ⁻¹] Density, ρ_{PET} [kg m ⁻³] Heat capacity, $c_{p,PET}$ [J kg ⁻¹ K ⁻¹] Melting temperature, T_m PET [K] Evaporation temperature, T_v PET [K] Latent heat of fusion, $H_{M,PET}$ [kJ/kg]	0.15 1450 2100 523 613 22

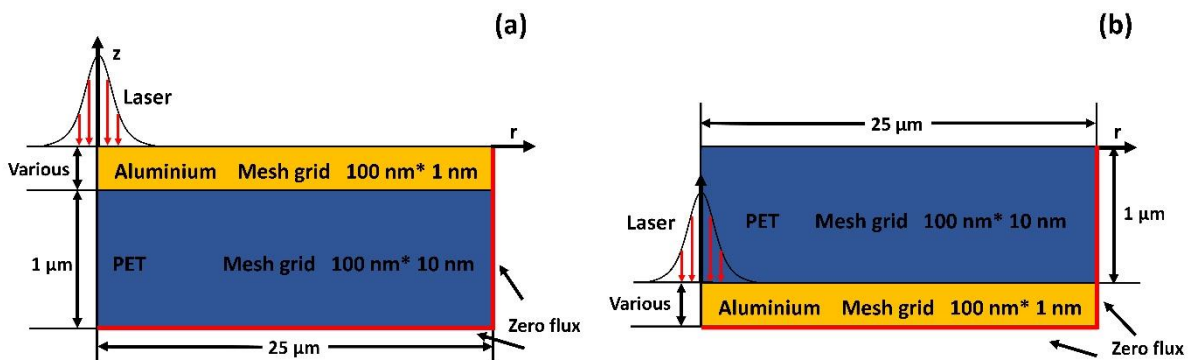


Figure 2. The geometric model of Al/PET film system and boundary conditions (a) front side ablation (b) rear side ablation.

4. Results and discussion

4.1 Experimental results

4.1.1 Estimated Film thickness

Five different optical density (OD) Al/PET films (OD= 2.5, 2.0, 1.5, 1.0, 0.5; BOBST Manchester Ltd) were measured, and the film thickness of aluminium could be estimated according to Beer-Lambert law [32]:

$$I_{out} = I_{in} e^{-\alpha t} \quad (12)$$

where t means film thickness, α is the absorption coefficient of aluminium at 1064 nm wavelength, I_{in} and I_{out} are the input and output power before and after the film, respectively. Using the collimated laser beam at 1064 nm, the film OD was measured experimentally and compared to the coated OD from the manufacturer. The Al/PET OD from the manufacturer is OD_l , the measured optical density OD_e and corresponding calculated aluminium film thickness t are listed in Table 2. To avoid misunderstanding the name of different films, we refer to the films by their given OD_l . The relationship between the input laser powers ($I_{in} = 5, 10, 15, 20$ and 25 mW) and output powers through the films is plotted in Figure 3.

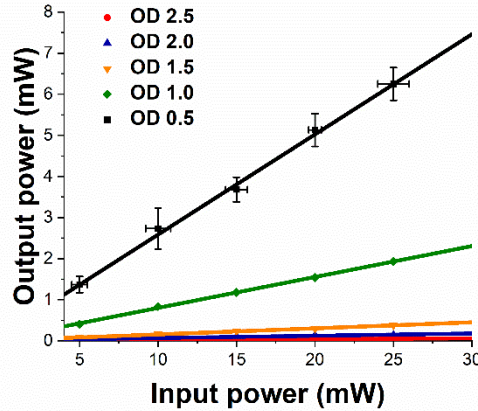


Figure 3. The plot of input power versus output power after the films with various quoted OD.

Table 2. Labelled OD, measured OD and estimated aluminium thickness

OD_l	0.5	1.0	1.5	2.0	2.5
OD_e	0.52 ± 0.03	1.06 ± 0.03	1.78 ± 0.02	2.10 ± 0.07	2.69 ± 0.01
t (nm)	9.9 ± 0.6	20.9 ± 0.2	33.9 ± 0.4	40.0 ± 1.4	51.2 ± 0.2

4.1.2 Experimental ablation thresholds

The front side (aluminium) and rear side (PET) single pulse ablation was investigated with a focused beam on the film surface. Figure 4 (a) - (e) shows the optical image of single-pulse ablation on the front side of different films under the same fluence, $F = 0.58$ J/cm². The ablated crater's radius at fixed fluence decreases as the film thickness increases. Note the high level of debris in Figure 4 (a) with the thinnest film. Curls around the spots appeared when film thickness was larger than 10 nm in Figure 4 (b) - (e). As PET is highly transparent at 1064nm, rear side ablation was also investigated. A comparison of optical images of the single-pulse ablation on the front and rear sides of $OD = 2.5$ Al/PET film with a fluence $F = 0.58$ J/cm² is shown in Figure 4 (e) and (f). The rear side ablated diameter (f) is larger than the front side ablated (e) diameter. This is likely due to the laser 'lift-off' effect on thin-film rear side ablation [9]. However, the delamination and the curls of the films on rear side exposure makes the front side ablation more suitable for precise machining of this thin film. The ablation threshold on different films was measured using the following two equations [33-35],

$$D^2 = 2\omega_0^2 \ln\left(\frac{F_0}{F_{th}}\right) \quad (13)$$

where D is the ablated crater diameter, ω_0 is the laser spot radius, F_{th} is the ablation threshold, and F_0 is the peak fluence which given by,

$$F_0 = \frac{2E_p}{\pi\omega_0^2} \quad (14)$$

where E_p is the pulse energy.

A plot of D^2 versus $\ln E_p$ is shown in Figure 5 (a), each data point was measured 5 times and error bars represents 1σ . A similar gradient ($2\omega_0^2$) of different films is observed, from which the focal spot radius (ω_0) was estimated along with the root mean square error yielding the $1/e^2$ focal spot radius to be $\omega_0 = 14.8 \pm 0.4 \mu\text{m}$. The front side ablation thresholds of different films are $F_{\text{th}}(f)_{0.5} = 0.021 \pm 0.008 \text{ J/cm}^2$, $F_{\text{th}}(f)_{1.0} = 0.051 \pm 0.010 \text{ J/cm}^2$, $F_{\text{th}}(f)_{1.5} = 0.078 \pm 0.014 \text{ J/cm}^2$, $F_{\text{th}}(f)_{2.0} = 0.093 \pm 0.009 \text{ J/cm}^2$ and $F_{\text{th}}(f)_{2.5} = 0.112 \pm 0.009 \text{ J/cm}^2$, as shown in Figure 5 (a). The rear side ablation thresholds of different films are $F_{\text{th}}(r)_{0.5} = 0.016 \pm 0.002 \text{ J/cm}^2$, $F_{\text{th}}(r)_{1.0} = 0.027 \pm 0.002 \text{ J/cm}^2$, $F_{\text{th}}(r)_{1.5} = 0.058 \pm 0.004 \text{ J/cm}^2$, $F_{\text{th}}(r)_{2.0} = 0.070 \pm 0.003 \text{ J/cm}^2$ and $F_{\text{th}}(r)_{2.5} = 0.102 \pm 0.004 \text{ J/cm}^2$, respectively. A comparison of ablation threshold versus aluminium film thickness at the front and rear side is shown in Figure 5 (b). The rear side ablation threshold is lower than the front side ablation threshold, consistent with the observation of ps ablation at 532 nm [4]. Also, there is a linear relationship between the film thickness and ablation threshold when the film thickness is lower than 50 nm. The damage threshold of PET film is calculated by ablating the pure PET film (after low fluence film ablation to remove the aluminium layer) yielding $F_{\text{th PET}} = 3.46 \text{ J/cm}^2$, again using a plot of D^2 versus $\ln E_p$, demonstrating a clear energy window for selective removal of the aluminium film without significant damage to the PET substrate.

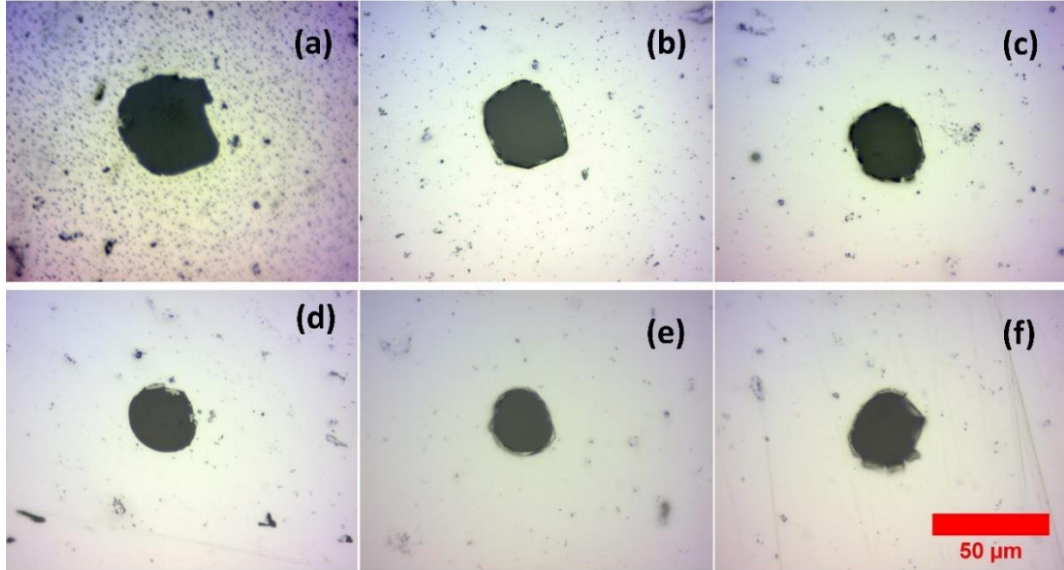


Figure 4. single pulse ablation under the same fluence $F = 0.58 \text{ J/cm}^2$ at different films (a) $\text{OD}_l = 0.5$, (b) $\text{OD}_l = 1.0$, (c) $\text{OD}_l = 1.5$, (d) $\text{OD}_l = 2.0$ and (e) $\text{OD}_l = 2.5$, front side ablation, (f) $\text{OD}_l = 2.5$ rear side ablation, with ‘curls’ over the edge

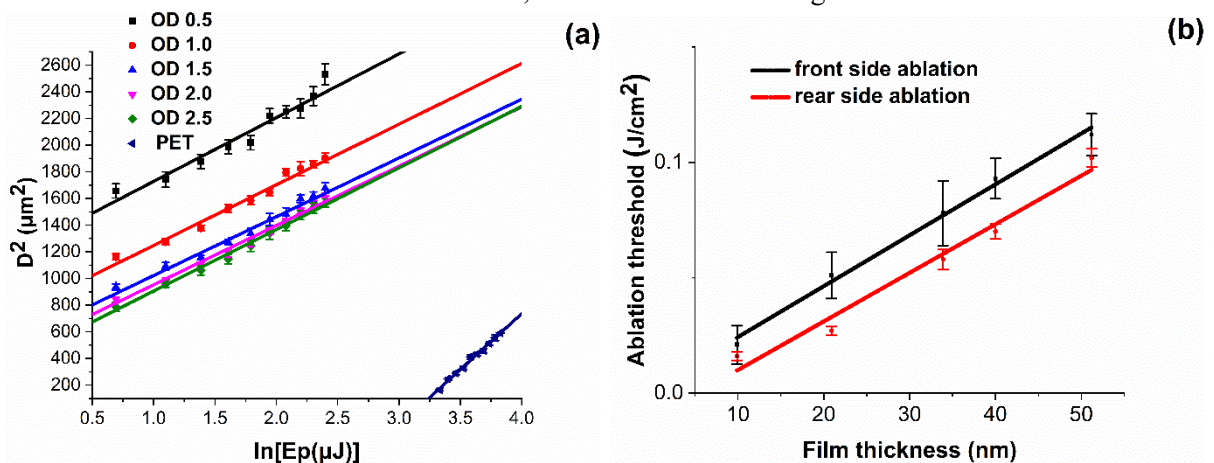


Figure 5. (a) Graph of squared ablation diameter D^2 versus $\ln E_p$ for the front side ablation of different aluminium thickness films and damage threshold of the PET film (b) the front and rear side ablation thresholds versus film thickness.

4.2 Numerical results

The Simulated 2D lattice temperature distributions of single-pulse ablation on OD 2.5 Al/PET film at time delay 100 ps are shown in Figure 6. The lattice temperature of front and rear side ablation at $F = 0.20 \text{ J/cm}^2$ are shown in Figure 6 (a) and (b), respectively. Similarly, the results at $F = 0.60 \text{ J/cm}^2$ are shown in Figure 6 (c) and (d). The lattice temperature is almost continuous for all simulations, except for an abrupt temperature change at the Al/ PET interface (black dash line), independent of depth in this simulation. This is because the thermal energy distribution can be considered homogenous when the film thickness is thin [9, 36]. The simulations with the OD 2.5 film are shown in Figure 6 (a) - (d) and appear physically realistic with a radial temperature gradient, a reflection of the incident Gaussian intensity distribution. The rapid temperature change at the interface is due to the thermal resistance between the aluminium and PET film, as the thermal conductivity of Al is around 1500 times higher than PET at room temperature. The red and yellow dotted contours represent the melting temperature of aluminium, $T_{\text{M Al}} = 933.5 \text{ K}$ and evaporation temperature of PET $T_{\text{V PET}} = 613 \text{ K}$, respectively.

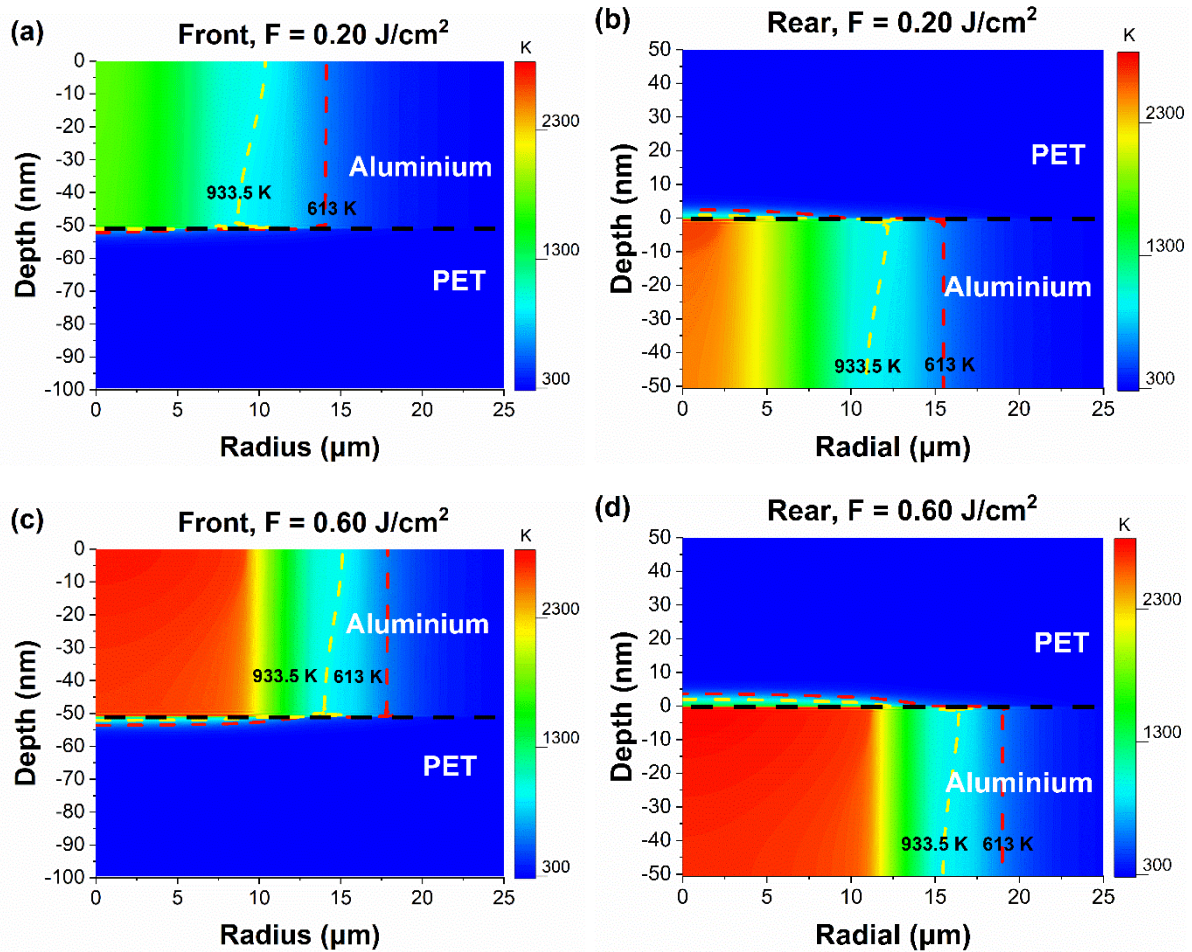


Figure 6. Simulated 2D lattice temperature distribution of single-pulse ablation of OD 2.5 Al/PET film at time delay 100 ps (a) front side ablation $F = 0.20 \text{ J/cm}^2$ (b) rear side ablation at 0.20 J/cm^2 (c) front side ablation at $F = 0.60 \text{ J/cm}^2$ (d) rear side ablation $F = 0.60 \text{ J/cm}^2$. The different lattice temperatures between the front and rear side ablation is due to the assumed absorptions, $A_f = 0.12$ and $A_r = 0.177$, respectively.

There is a different temperature gradient radius between the front and rear side simulations, with aluminium melting crater (yellow contour) $w_0 \sim 10 \mu\text{m}$ at Al top surface in Figure 6 (a) and $w_0 \sim 12 \mu\text{m}$ at Al/PET interface in Figure 6 (b). This is connected with the different laser absorption assumed in front and rear side ablation, as $A_f = 0.12$ and $A_r = 0.177$. However, the aluminium lattice temperature

in Figure 6 (a) and (b) is still lower than the evaporation temperature of aluminium $T_{v Al} = 2743$ K at fluence $F = 0.2$ J/cm² and 100 ps, which already exceeds the experimental ablation threshold $F_{th}(f)_{2.5} = 0.112 \pm 0.009$ J/cm² and $F_{th}(r)_{2.5} = 0.102 \pm 0.004$ J/cm², reflecting the asymmetric energy coupling to the Al/PET interface between front and rear side ablation. These very low thresholds show that there is an increase in ablation efficiency due to the PET substrate. The electron and lattice temperature of different OD's Al/PET films were investigated from time $t = 0$ to $t = 100$ ps time delay.

All films are irradiated at the same fluence ($F = 0.20$ J/cm²), and the time-resolved electron and lattice temperature change are simulated at the laser beam centre (0,0), illustrated in Figure 7. Different electron and lattice temperatures are observed, while peak T_e occurs just after the 10 ps pulse has been absorbed. In front side ablation, thermal equilibrium is achieved within approximately 25 ps, Fig. 7 (a). The highest electron temperature appears at the thinnest film (OD 0.5, $t \sim 10$ nm) with $T_e \sim 7,600$ K. As the aluminium film thickness increases, peak electron temperatures decrease and with OD 1.0 ($t \sim 20$ nm) T_e drops to 5,650 K. When aluminium film thickness is larger than 30 nm, the highest electron temperature of the film, $T_e \sim 4,000$ K in OD 1.5, 2.0 and 2.5. It takes ~ 25 ps for electrons and lattice to reach the thermal equilibrium in all cases.

In rear side ablation, Figure 7 (b), the highest electron temperature $T_e \sim 10,000$ K at OD 0.5, dropping to $\sim 7,800$ K at OD 1.0, and finally close to 5,500 K. However, the lattice temperature in rear side ablation have not reached thermal equilibrium within 100 ps for all cases. This is because the lattice temperature, detected at the Al/PET interface, point (0,0), can be considered as the lattice temperature of PET. The slow PET lattice temperature rise is due to its very low thermal diffusivity (and higher heat capacity) compared to aluminium and requires much more time to reach equilibrium, approximately 2 ns.

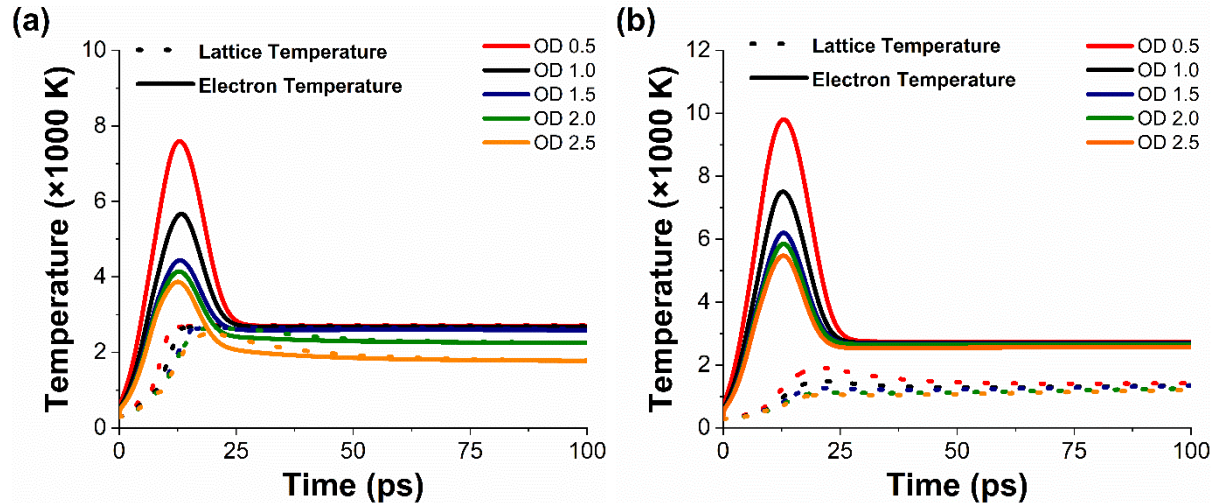


Figure 7. Time-resolved electron and lattice temperature evaluation of different Al/PET films under a fluence $F = 0.20$ J/cm² at laser centre position (0,0) (a) front side ablation (b) rear side ablation, point (0,0) at Al/PET interface

The spatial lattice temperature distribution along the film axis under the fluence $F = 0.20$ J/cm² at 100 ps delay is shown in Figure 8. The Al film temperature with depth (for a given OD) is almost constant in all cases, except a small temperature change in the rear side ablation of OD 2.5 film, Figure 8 (a) and (b). As expected, there is a steep temperature gradient between the Al/PET interface, and the temperature oscillates near the Al/PET interface in both front/rear side ablation cases. The sudden electron-lattice coupling change near the Al/PET interface might contribute to the temperature oscillation, or this may be an artefact of simulation.

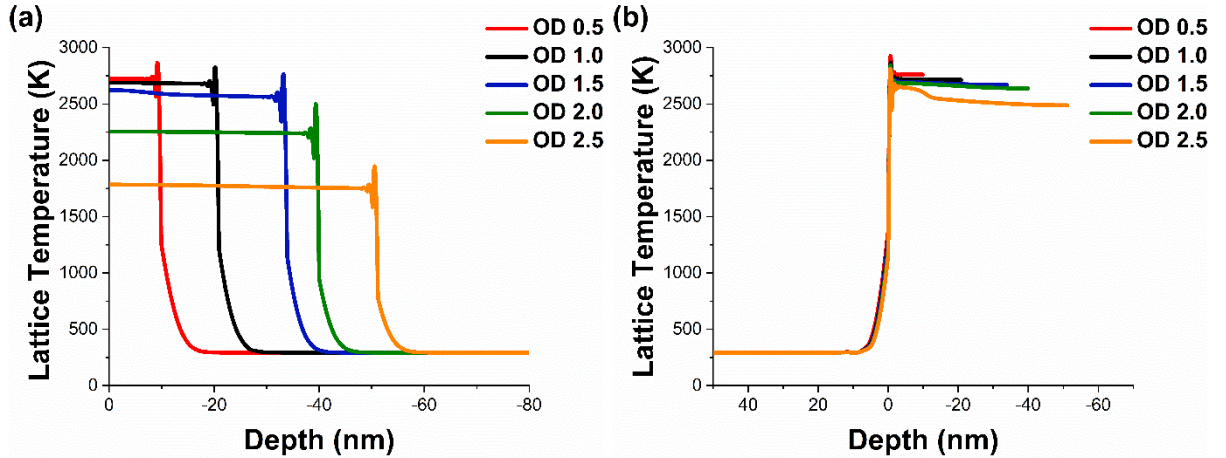


Figure 8. Simulated lattice temperature at Fluence $F = 0.2 \text{ J/cm}^2$ and 100 ps delay time (a) front side ablation of Al/PET films (b) rear side ablation of Al/PET films

4.3 Experimental and simulation results comparison

To investigate how the PET substrate improves the ablation efficiency, the lattice temperature of aluminium and PET at the laser spot centre axis ($r = 0$) on a time scale of 1000 ps were investigated. The ablation threshold is assumed to be the fluence that heats the PET to its evaporation temperature, while the aluminium remains in the liquid phase. This, we believe, is the point at which ablation will occur. For example, the OD 2.5 film front side ablation, the lattice temperature of PET at Al/PET interface (0, -51.2) and close to the bottom surface of the aluminium (0, -48) under the different fluences ($F = 0.07, 0.08, 0.091, 0.10 \text{ J/cm}^2$) is shown in Figure 9 (a). Note that the aluminium lattice temperature is always well below the evaporation point (2743K). However, it shows a fast transient, exceeding the melting point (933K) at early times, then reaching a steady state after approximately 300 ps. Also, the PET temperature reaches its evaporation point (613 K) between 300-400 ps time delay, increasing with time. With the two conditions met, $F_{\text{th}}(f_{\text{sim}})_{2.5} = 0.091 \text{ J/cm}^2$ is the simulated ablation threshold of the front side ablation of the OD 2.5 film, which is close to the experimental ablation threshold $F_{\text{th}}(f)_{2.5} = 0.112 \pm 0.0091 \text{ J/cm}^2$. Figure 9 (b) shows the temperature of the OD 0.5 film, and one can see that a fluence $F = 0.02 \text{ J/cm}^2$ is not sufficient to melt the aluminium while $F_{\text{th}}(f_{\text{sim}})_{0.5} = 0.028 \text{ J/cm}^2$ achieves both Al melting and PET evaporation. This value compares favourably with the experimental value, $F_{\text{th}}(f)_{0.5} = 0.021 \pm 0.008 \text{ J/cm}^2$.

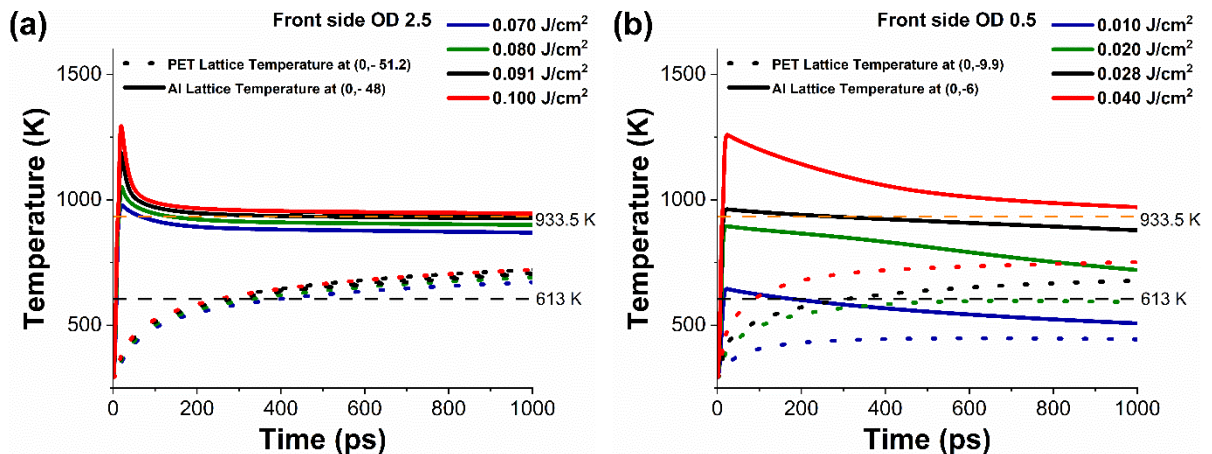


Figure 9. The lattice temperature of Al and PET at laser spot centre on a time scale of 1000 ps (a) OD 2.5 front side ablation at point (0, -48) and (0, -51.2) under various fluence $F = 0.07, 0.08, 0.091, 0.10 \text{ J/cm}^2$ (b) OD 0.5 front side ablation at point (0, -6) and (0, -9.9) under various fluence $F = 0.01, 0.020, 0.028, 0.04 \text{ J/cm}^2$. Orange dash line represent the Al melting temperature $T_M \text{ Al} = 933.5 \text{ K}$ and black dash line represents the evaporation temperature of the PET $T_v \text{ PET} = 613 \text{ K}$

The front/rear side experimental ablation thresholds (black square) and simulated thresholds (red dot) are shown in Figure 10 (a) and (b) on a log-log scale with excellent agreement. For comparison, the ablation thresholds (blue triangle) based on the requirement of complete evaporation of the aluminium films support the assumption that the film only needs to reach its melting point combined with the PET reaching its evaporation (decomposition) point. The discrepancy between theory and experiment for the thicker films may be due to limited knowledge of the temperature dependence of physical parameters used in modelling (Table 1). Alternatively, there may be an additional loss in laser-material coupling (in liquid aluminium) due to increased transient reflectivity (during the pulse) from the temporal change in complex refractive index and not considered here [37]. This will be more significant for the thicker films whose thickness $t \geq$ optical penetration depth $l_{\text{opt}} \sim 1/\alpha = \lambda/(4\pi k) = 8.8 \text{ nm}$ at 1064 nm and where a vertical temperature gradient develops, while it will be less significant for thin films where heat diffusion essentially eliminates vertical temperature gradients.

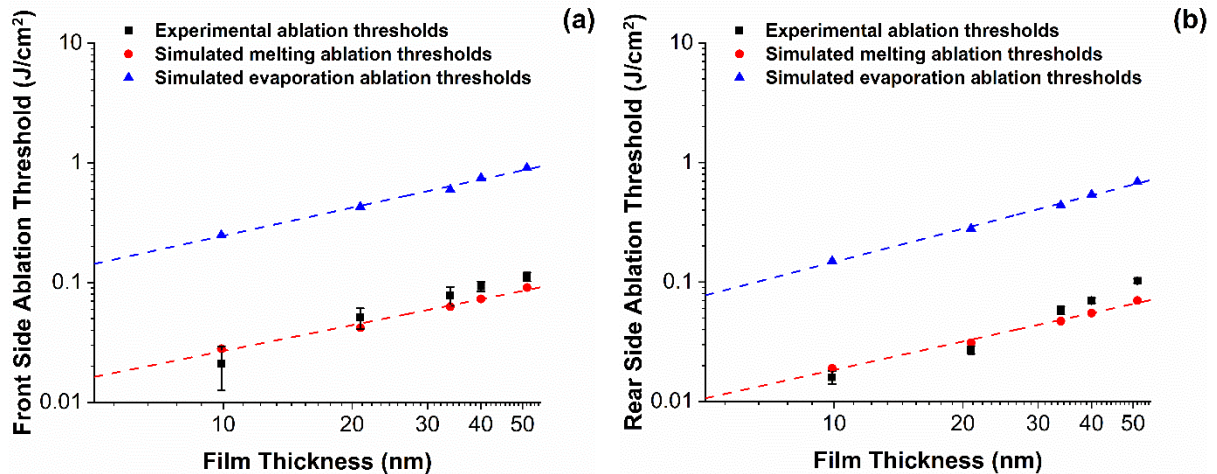


Figure 10. The log-log plot of ablation threshold versus film thickness of the experimentally observed (black square), simulated ablation thresholds (red dot) and the ablation thresholds (blue triangle) based on the requirement of complete evaporation of the aluminium films (a) front side ablation (b) rear side ablation

4.4 Single/Multi-beams processing

With the measured and simulated ablation thresholds of Al/PET thin film, the OD 2.0 films and fluence $F = 0.58 \text{ J/cm}^2$, which can easily machine the Al film without damaging the PET substrate, are chosen for laser micro-machining. In this case, the relationship between pulse overlap N and scanning speed v on OD 2.0 film under the fluence $F = 0.58 \text{ J/cm}^2$ in Figure 11 shows that the processing speed plays an important role in final machining results. The overview of machining results is shown in Figure 11 (a). Cracks appear around the line structure when scan speed is relatively low ($v < 10 \text{ mm/s}$, Figure 11 (b) - (c)). This is likely due to the residual heat effect during processing under a relatively high pulse overlap O_R , which can be calculated by $O_R = \left(1 - \frac{v}{2\omega_0 f}\right) \times 100\%$ [38], where v represents the scan speed, ω_0 is the beam radius and f is the pulse repetition rate. The heat flow and stress accumulate and damages the film edges. A straight and clean line structure can be seen with scan speed at 15 mm/s and 30 mm/s (Figure 11 (e)). Furthermore, with increasing scan speed, the line surface becomes less smooth and finally becomes discrete with multiple spots, as shown in Figure 11 (f) – (g).

A phase-only spatial light modulator (SLM, Hamamatsu X10468-03) addressed with appropriate CGHs was used to generate multi-beams which can improve the processing efficiency of the Al /PET thin films. A 5×5 array beam is created using a binary Dammann grating hologram on the SLM [39]. The CGH and low-intensity beams monitored on the Spyroicon CCD camera are shown in Figure 12 (a) and (b), respectively. The higher energy central spot in Figure 12 (b) is due to the zero-order of the CGH, while the surrounding uniform intensity spots of the 5×5 array are the first-order diffracted beams.

Note that there are four ghost beams on the central x and y-axis of spots, and only two ghosts were shown here due to the size of the Spyricon CCD. Pulse energy $E = 2 \mu\text{J}$ per spot ($F = 0.58 \text{ J/cm}^2$) and 15 mm/s scan speed was selected from the experiments of single line processing. A chessboard pattern using the 5×5 spot array was scribed and shown in Figure 12 (c). The spots in the dashed square in Figure 12 (c) are the 5×5 spot array, and the other 4 are the ghost spots. The higher magnification of Figure 12 (c) is shown in Figure 12 (d) and (e), and ~ 25 times processing time efficiency can be achieved by using parallel beam processing compared with single beam scribing. With a single overscan, clean patterning was observed with no PET damage, and the processing rate was $R \sim 0.11 \text{ cm}^2/\text{sec}$. Applications of Al/PET laser micro-patterning include the creation of AC luminescent electro-displays displays [4] and potentially useful as capacitive strain sensors which have interdigitated electrodes .

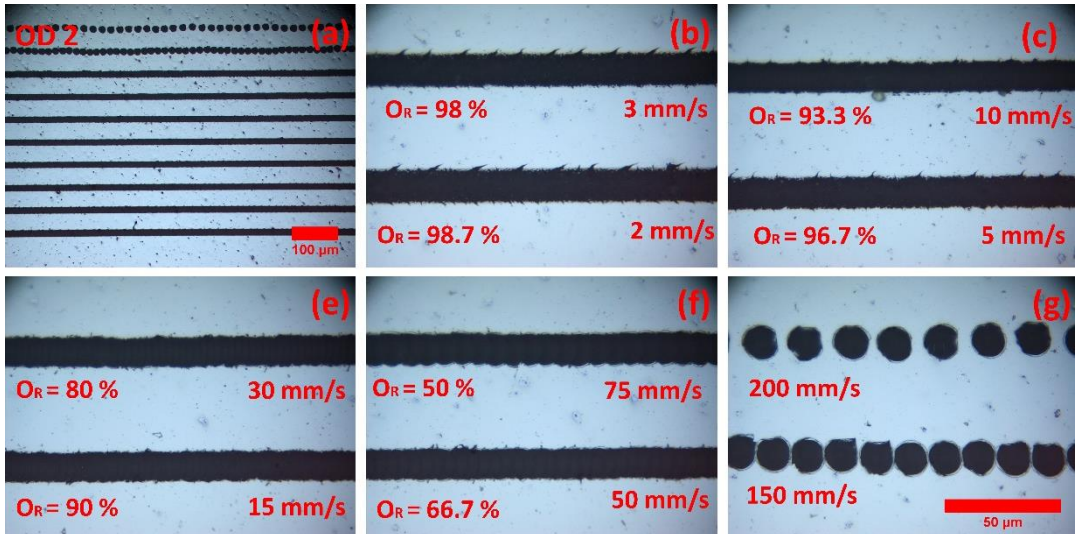


Figure 11. Optical images of single beam front surface scribing on OD 2.0 Al/PET film under the fluence $F = 0.58 \text{ J/cm}^2$. The overview of single line patterning versus scan speed is shown in a). More detailed figures with the same scale at corresponding processing parameters are listed in (b)-(g)

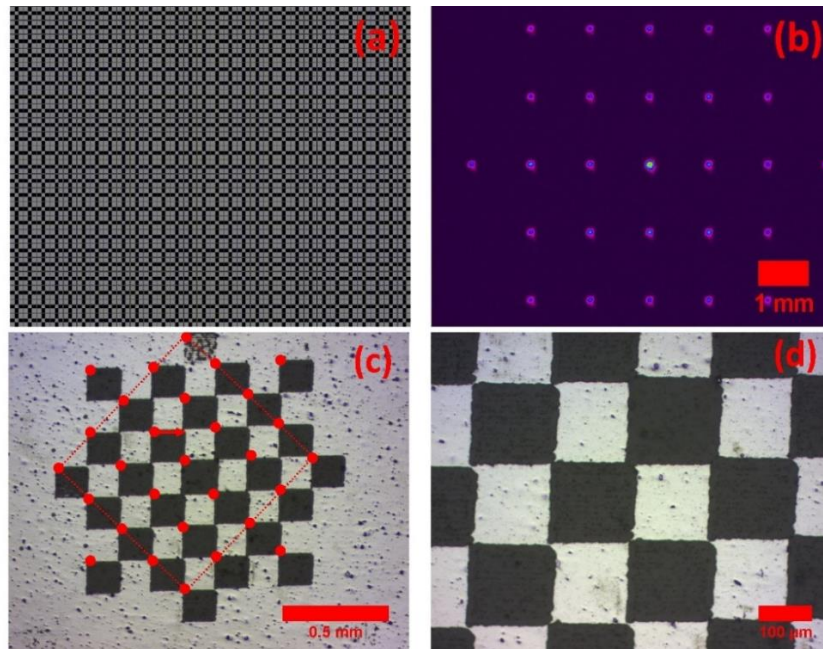


Figure 12. (a) CGH generated by using binary Dammann grating (b) CCD camera image of a single laser split into 5×5 arrays. The array is uniform, apart from the higher energy zero-order spot on the centre, while ghost beams also appear on either side of the central spot line (c) 5×5 multi-spots array thin-film patterning of the chessboard. The spots in the dashed square are the 5×5 spot array, while the other 4 are the ghost spots (d) magnified optical image of the chessboard pattern.

5. Conclusion

An experimental and numerical study on the single pulse ablation of different optical density Al/PET films is presented. Both electron and lattice temperatures of the aluminium film and PET substrate were modelled with time, showing that electron temperatures in aluminium, as expected, well exceed lattice temperatures at early times, and a nonequilibrium situation exists for approximately 30 ps, film dependent. The PET response time to reach the evaporation temperature is typically ~ 300 ps, as a consequence of the very low thermal diffusivity. Regarding the ablation mechanism, if we assume the aluminium lattice reaches melting point along with the requirement that PET temperature reaches its evaporation (decomposition) temperature, this is the threshold at which aluminium film ablation occurs and applies to both front and rear film ablation. The excellent agreement between the experiment and simulation supports the assumption that the decomposing polymer substrate increases the ablation efficiency through laser ‘lift-off’. Ablation thresholds are a factor of 10 lower than the fluence required to evaporate the films completely confirmed by modelling. The observed wide processing window with 10 ps laser ablation allowed the demonstration of multi-beam parallel processing with the aid of an SLM which can dramatically increase the processing efficiency.

Acknowledgements

We would like to thank the supplier of the thin films, BOBST, Manchester.

Data availability statement

The data that support the findings of this study are available from the corresponding author upon reasonable request.

Declaration of Competing Interest

The authors declare that they have no known competing financial interests or personal relationships that could have appeared to influence the work reported in this paper.

CRediT authorship contribution statement

Tong Zhou: Conceptualisation, Methodology, Investigation, Software, Validation, Data curation Writing –original draft. **Zheng Fang:** Methodology, Software, Validation, Data curation. **Walter Perrie:** Conceptualisation, Methodology, Supervision, Formal analysis, Validation, Writing –review & editing. **Yang Fei:** Software, Validation, Data curation. **Stuart Edwardson:** Resource, Supervision, Writing –review & editing. **Geoff Dearden:** Resource, Supervision, Writing –review & editing.

References

- [1] M. Park, B.H. Chon, H.S. Kim, S.C. Jeoung, D. Kim, J.-I. Lee, H.Y. Chu, H.R. Kim, Ultrafast laser ablation of indium tin oxide thin films for organic light-emitting diode application, Optics and Lasers in Engineering, 44 (2006) 138-146.
- [2] C.-Y. Chen, T.-L. Chang, Multilayered structuring of thin-film PV modules by ultrafast laser ablation, Microelectronic Engineering, 143 (2015) 41-47.
- [3] J. Mur, J. Petelin, J. Schille, U. Loeschner, Ultra-fast laser-based surface engineering of conductive thin films, Applied Surface Science, 509 (2020) 144911.

- [4] Y. Jin, W. Perrie, P. Harris, O. Allegre, K. Abrams, G. Dearden, Patterning of Aluminium thin film on polyethylene terephthalate by multi-beam picosecond laser, *Optics and Lasers in Engineering*, 74 (2015) 67-74.
- [5] L. Overmeyer, J. Duesing, O. Suttmann, U. Stute, Laser patterning of thin film sensors on 3-D surfaces, *CIRP annals*, 61 (2012) 215-218.
- [6] X. Yu, J. Ma, S. Lei, Femtosecond laser scribing of Mo thin film on flexible substrate using axicon focused beam, *Journal of Manufacturing Processes*, 20 (2015) 349-355.
- [7] G. Spiecker, Excimer lasers support industrial micromachining diversity, *Laser Technik Journal*, 4 (2007) 36-39.
- [8] G. Heise, M. Domke, J. Konrad, S. Sarrach, J. Sotrop, H.P. Huber, Laser lift-off initiated by direct induced ablation of different metal thin films with ultra-short laser pulses, *Journal of Physics D: Applied Physics*, 45 (2012) 315303.
- [9] M. Domke, L. Nobile, S. Rapp, S. Eiselen, J. Sotrop, H.P. Huber, M. Schmidt, Understanding thin film laser ablation: The role of the effective penetration depth and the film thickness, *Physics Procedia*, 56 (2014) 1007-1014.
- [10] S. Zhou, K. Zhao, H. Shen, Ablation of gold film on different substrates by ultrafast laser, *Optics & Laser Technology*, 132 (2020) 106495.
- [11] C. McDonnell, D. Milne, C. Prieto, H. Chan, D. Rostohar, G. O'Connor, Laser patterning of very thin indium tin oxide thin films on PET substrates, *Applied Surface Science*, 359 (2015) 567-575.
- [12] B. Mueller, B. Rethfeld, Nonequilibrium electron–phonon coupling after ultrashort laser excitation of gold, *Applied Surface Science*, 302 (2014) 24-28.
- [13] S. Anisimov, B. Kapeliovich, T. Perelman, Electron emission from metal surfaces exposed to ultrashort laser pulses, *Zh. Eksp. Teor. Fiz.*, 66 (1974) 375-377.
- [14] K.K. Kumar, G. Samuel, M. Shunmugam, Theoretical and experimental investigations of ultra-short pulse laser interaction on Ti6Al4V alloy, *Journal of Materials Processing Technology*, 263 (2019) 266-275.
- [15] X. Wang, Y. Huang, C. Li, B. Xu, Numerical simulation and experimental study on picosecond laser ablation of stainless steel, *Optics & Laser Technology*, 127 (2020) 106150.
- [16] Q. Li, H. Lao, J. Lin, Y. Chen, X. Chen, Study of femtosecond ablation on aluminum film with 3D two-temperature model and experimental verifications, *Applied Physics A*, 105 (2011) 125-129.
- [17] M. Olbrich, E. Punzel, R. Roesch, R. Oettking, B. Muhsin, H. Hoppe, A. Horn, Case study on the ultrafast laser ablation of thin aluminum films: dependence on laser parameters and film thickness, *Applied Physics A*, 122 (2016) 215.
- [18] T. Qiu, T. Juhasz, C. Suarez, W. Bron, C. Tien, Femtosecond laser heating of multi-layer metals—II. Experiments, *International Journal of Heat and Mass Transfer*, 37 (1994) 2799-2808.
- [19] H. Wang, W. Dai, L.G. Hewavitharana, A finite difference method for studying thermal deformation in a double-layered thin film with imperfect interfacial contact exposed to ultrashort pulsed lasers, *International Journal of Thermal Sciences*, 47 (2008) 7-24.
- [20] A. Majumdar, P. Reddy, Role of electron–phonon coupling in thermal conductance of metal–nonmetal interfaces, *Applied Physics Letters*, 84 (2004) 4768-4770.
- [21] B. Shi, X. Tang, T. Lu, T. Nakayama, Y. Li, J. Zhou, Interfacial thermal conductance at metal–nonmetal interface via electron–phonon coupling, *Modern Physics Letters B*, 32 (2018) 1830004.
- [22] X. Wang, C. Ma, C. Li, M. Kang, K. Ehmann, Influence of pulse energy on machining characteristics in laser induced plasma micro-machining, *Journal of Materials Processing Technology*, 262 (2018) 85-94.
- [23] J. Chen, D. Tzou, J. Beraun, A semiclassical two-temperature model for ultrafast laser heating, *International journal of heat and mass transfer*, 49 (2006) 307-316.
- [24] A.D. Rakić, Algorithm for the determination of intrinsic optical constants of metal films: application to aluminum, *Applied optics*, 34 (1995) 4755-4767.
- [25] L.A. Akashev, V.I. Kononenko, Optical properties of liquid aluminum and Al–Ce alloy, *High Temperature*, 39 (2001) 384-387.

- [26] G. Hass, J.E. Waylonis, Optical constants and reflectance and transmittance of evaporated aluminum in the visible and ultraviolet, *JOSA*, 51 (1961) 719-722.
- [27] M. Kandyla, Ultrafast dynamics of the laser-induced solid-to-liquid phase transition in aluminum, Ph. D. Thesis, (2006).
- [28] X. Zhang, J. Qiu, X. Li, J. Zhao, L. Liu, Complex refractive indices measurements of polymers in visible and near-infrared bands, *Applied optics*, 59 (2020) 2337-2344.
- [29] Y. Tokunaga, H. Kobayashi, Y. Ishimaru, K. Aizawa, J. Hirama, Thermal diffusivities of commercial transparent polymer films measured using laser induced thermal wave, *Acoustical science and technology*, 31 (2010) 288-292.
- [30] A. Jain, A.J. McGaughey, Thermal transport by phonons and electrons in aluminum, silver, and gold from first principles, *Physical Review B*, 93 (2016) 081206.
- [31] Z. Lin, L.V. Zhigilei, V. Celli, Electron-phonon coupling and electron heat capacity of metals under conditions of strong electron-phonon nonequilibrium, *Physical Review B*, 77 (2008) 075133.
- [32] D.F. Swinehart, The beer-lambert law, *Journal of chemical education*, 39 (1962) 333.
- [33] J. Liu, Simple technique for measurements of pulsed Gaussian-beam spot sizes, *Optics letters*, 7 (1982) 196-198.
- [34] S.-F. Tseng, C.-H. Liao, Investigation of interactions between ultrafast laser beams and screen-printed silver nanopaste films, *Applied Surface Science*, 512 (2020) 144696.
- [35] S.-F. Tseng, C.-C. Huang, Investigation of interactions between high pulsed ultraviolet lasers and composite graphene/AgNWs films, *Applied Surface Science*, 570 (2021) 151060.
- [36] J.L. Hostetler, A.N. Smith, D.M. Czajkowsky, P.M. Norris, Measurement of the electron-phonon coupling factor dependence on film thickness and grain size in Au, Cr, and Al, *Applied optics*, 38 (1999) 3614-3620.
- [37] J. Winter, S. Rapp, M. Spellauge, C. Eulenkamp, M. Schmidt, H.P. Huber, Ultrafast pump-probe ellipsometry and microscopy reveal the surface dynamics of femtosecond laser ablation of aluminium and stainless steel, *Applied Surface Science*, 511 (2020) 145514.
- [38] S.-F. Tseng, Y.-S. Chen, Surface microtexturing of Ti-6Al-4V and SS316L alloys using high pulsed fiber lasers for improving the adhesive bonded performance, *Optics & Laser Technology*, 143 (2021) 107349.
- [39] U. Krackhardt, N. Streibl, Design of Dammann-gratings for array generation, *Optics communications*, 74 (1989) 31-36.